An enclosed live-imaging platform to reveal ultrasound-inflicted mechanolysis and wound healing response

Ziyue Bai[1], Zaimeng Li[2], and Yue Shao[1,*]

[1] Institute of Biomechanics and Medical Engineering, Department of Engineering Mechanics, School of Aerospace Engineering, Tsinghua University, Beijing 100084, China; [2] Institute of Fluid Mechanics, Department of Engineering Mechanics, School of Aerospace Engineering, Tsinghua University, Beijing 100084, China

* Correspondence should be addressed to Y. Shao (yshao@tsinghua.edu.cn)

ABSTRACT

Focused ultrasound (FUS) technology as a non-invasive therapy has been widely adopted in medical and life science research. Although various physical and biological effects of FUS have been well-documented, there is still a lack of understanding and direct evidence on the biological mechanism of therapeutic cell ablation caused by high-intensity ultrasound (HIFU) and the subsequent wound healing responses. Herein, this study designed and built an enclosed cell culture device that can synergistically combine non-invasive FUS stimulation and long-term live-cell imaging, serving as an in vitro platform to explore both short and long-term biological effects of ultrasound. Further, the process, mechanism and wound healing response of cell ablation induced by HIFU were studied, revealing a unique mechanism, termed ultrasound-inflicted mechanolysis, that is mediated by growing cavitation air bubbles under confined contact with cells. This discovery provides a previously unappreciated mechanism for understanding the biomechanical principles of ultrasound-based ablative therapy. We also found a post-ablation phantom layer (PAPL) remaining attached to neighboring live cell monolayer after HIFU stimulation. Such PAPL serves as a guiding cue for collective cell migration during post-ablation wound healing process, thereby providing a biomimetic model for studying wound healing after HIFU-inflicted damage. Together, the findings of this study might provide theoretical and technological basis for advancing our understanding of the biological effects of ultrasound-based ablative therapy and inspiring clinically relevant applications in the future.

INTRODUCTION

In recent years, focused ultrasound (FUS) technology has attracted extensive attention as a non-invasive therapeutic modality and has rapidly advanced in various research areas[1-3]. Currently, the most common application of therapeutic FUS is in the ablation of tumors[4, 5]. Furthermore, FUS exhibits deep penetration and high spatial precision in comparison to other therapeutic physical stimuli. Low-frequency focused ultrasound (frequency < 1MHz) can non-invasively focus within the cranial region[6] and it can be combined with other therapeutic modalities such as microbubbles and phase-change liquid droplets[7]. By promoting transcellular endocytosis, inducing endothelial cell membrane opening, forming cavities or channels within the cytoplasm, and opening tight junctions between endothelial cells, FUS facilitates the delivery of therapeutic agents, *e.g.*, cisplatin[8], doxorubicin[9, 10], mistletoe lectin-1 (ML1)[11], trastuzumab[12], and genetic materials[13] across the blood-brain barrier (BBB)[14, 15] or blood-tumor barrier (BTB)[16-18]. On neuroregulation, FUS can either inhibit or activate neural activity[19-21], showing significant potential in analgesia[22]. Its stimulation of the hepatic portal venous plexus holds promise as a non-pharmacological treatment for glucose homeostasis dysregulation[23]. Moreover, FUS has been applied in thrombolysis[24], as well as in therapeutic research related to inflammation[25, 26]. Overall, FUS-based therapeutic techniques offer vast avenues for clinically relevant applications.

The therapeutic principle of FUS technology is based on the energy accumulation generated when ultrasound waves are focused on specific areas in tissues, leading to thermal or mechanical effects. Subsequently, a series of biological effects are induced to achieve therapeutic objectives. The thermal effect of focused ultrasound refers to the higher energy accumulation at the focal point, causing a significant temperature increase in the targeted tissue compared to non-focal tissue. Different temperature elevation can achieve varying regulatory effects[27, 28]. For instance, using low-intensity focused ultrasound (LIFU) can mildly increase the temperature (e.g., a rise of 2-6℃) of the targeted

63 tissue as a form of local hyperthermia[29]. On the other hand, employing high-intensity focused ultrasound
64 (HIFU) for a short duration can heat the targeted tissue to a high temperature (above 55°C), leading to
65 coagulative necrosis and "thermal ablation" of tissue. The mechanical effects of FUS primarily include
66 cavitation effects, which are divided into stable cavitation and inertial cavitation. Stable cavitation refers
67 to the stable oscillation of microbubbles in the focal region under the effect of pressure waves. Inertial
68 cavitation involves the drastic volume changes of microbubbles under the influence of strong pressure
69 waves, ultimately leading to their rupture and generating shock waves[30]. Despite considerable research
70 on the physical effects of FUS, the investigation into the biological effects mechanism such as cell
71 ablation induced by HIFU, and the subsequent wound healing response, remains limited. This hinders a
72 comprehensive understanding of the mechanisms underlying HIFU therapy and limits improvements
73 and optimizations in ultrasound therapeutic methods. Therefore, it is critically needed to explore the
74 mechanism of HIFU-induced cell ablation and associated wound healing responses.

75 To investigate the mechanisms of ultrasound therapy, *e.g.*, HIFU-induced cell ablation, it is
76 essential to develop experimental models that can simulate multicellular damage and repair processes
77 under ultrasound treatment in vitro. Traditionally, for in vitro studies on the biological effects of
78 ultrasound, researchers would typically expose cells to FUS treatment and then observe them under a
79 microscope[31-33]. This method is relatively simple and convenient but lacks real-time observation of cell
80 responses during FUS stimulation, which is necessary for studying short-term cell responses. Currently,
81 real-time monitoring devices for studying ultrasound-induced responses mainly rely on either an upright
82 or an inverted microscope. For example, Zhihai *et al*.[34] integrated a FUS device with an upright
83 microscope, placing the focused ultrasound transducer beneath the culture dish at a 45-degree angle.
84 When cells were stimulated with FUS, the incident sound waves were focused to the bottom of the
85 culture chamber through a waveguide material, then reflected at a right angle to reach an absorber.

86 Simultaneously, real-time imaging was performed by immersing the objective into the upright-placed
87 cell culture dish during stimulation. Recently, Yao-Shen *et al*.[35] combined a FUS device with an
88 inverted microscope, with the FUS transducer was immersed vertically into the cell culture medium.
89 However, these setups required immersing the objective lens or ultrasound transducer into an open cell
90 culture environment, leading to a significant risk of contamination. Despite that they might be suitable
91 for short-term experiments (0-30 minutes), they are insufficient to support continuous studies on the cell
92 ablation mechanisms and subsequent wound healing responses induced by HIFU. This hinders the
93 exploration and understanding of relevant mechanisms. Therefore, it is imperative to develop new
94 technologies that integrate non-invasive ultrasound stimulation, real-time live-cell imaging, and long-
95 term cell culture into a single platform. This is a key technical challenge that this study aims to address.
96 Herein, this study has designed and constructed a fully enclosed cell culture device (ECCD)
97 capable of simultaneously achieving non-invasive ultrasound stimulation and long-duration live-cell
98 imaging. This device serves as an experimental platform for exploring the biological effects of FUS.
99 Unlike previously reported open culture systems, this platform allows for real-time and programmable
100 FUS stimulation of cells in the target region, while also enabling long-term, online monitoring of
101 cellular responses using an inverted microscope. We applied this platform to investigate both short and
102 long-term cellular responses during and after HIFU-induced cell ablation, and provided direct
103 experimental evidence and insights into previously unappreciated biomechanical mechanisms
104 underlying the cell damage and wound healing involved in FUS-based ablative therapy.
105

106 **RESULTS**

107 **Design of an enclosed cell culture device compatible with FUS stimulation and long-term live-**
108 **cell imaging**

109 In order to simultaneously achieve non-invasive FUS stimulation and long-term live-cell
110 imaging, this study established an enclosed cell culture device (ECCD). Through optimized design of
111 the acoustic path, acoustic windows, and sound-absorbing materials, the device enables FUS to act on a
112 focal cell culture area at the bottom of the cell culture device (**Fig. 1a**). Meanwhile, real-time imaging
113 captures changes and responses of the cultured cells in this region. Specifically, this design allows the
114 FUS to be emitted from the transducer, reach the outside of the cell culture device via the coupling
115 device, pass through the acoustic window, and further propagate in the cell culture medium. Ultrasonic
116 waves then focus at the bottom of the ECCD, where a glass coverslip for cell culture is horizontally
117 positioned. The axis of the ultrasound cone forms a 45-degree angle with coverslip, and are
118 subsequently reflected at a 45-degree angle. Such reflected waves pass through the exit acoustic window
119 and are absorbed by a sound-absorbing material attached to the window, thereby avoiding additional
120 reflections that may affect the focused acoustic field within the cell culture device.
121 The ECCD is assembled from multiple components. To meet requirements for FUS stimulation
122 and routine cell culture, we adopted a four-sided pyramid structure (**Fig. 1b**). The left and right sides of
123 the device are inclined at 45-degree against the bottom surface, with circular and rectangular windows
124 are opened on each, henceforth referred to as "entrance acoustic window (EnAW)" and "exit acoustic
125 window (ExAW)", respectively. Both acoustic windows are sealed with 1 mm thick sheet of acoustically
126 transparent material. This allows the FUS beam to transmit with extremely low loss along the expected
127 acoustic path while avoiding direct contact between the ultrasound transducer and the liquid inside the
128 culture device. A circle of grooves is extended from the inner edge of the EnAW and ExAW for
129 positioning and stabilizing the acoustically transparent sheet. To ensure correct positioning and light
130 contact of the ultrasound transducer coupler and the EnAW, a set of protruding keys were manufactured
131 at the inner rim of the EnAW to restrict the translational movement of the coupler. A circular opening

132 and recess structure are made at the bottom of the ECCD to allow the attachment of a coverslip for cell
133 culture (**Fig. 1b**).

134 Considering the relatively large size of the FUS transducer, a coupler is required to integrate it
135 with the ECCD. To match the shape of the ultrasound transducer and the ultrasound cone, the coupler is
136 designed to contain a conical head (**Fig. 1c&d**), which has a circular opening covered with a 1 mm thick
137 acoustically transparent sheet. The coupler also features a set of protruding keys complementary to those
138 on the rim of the EnAW of ECCD, ensuring the centered assembly and tight fit between them (**Fig. 1e**).
139 During operation, the coupler is filled with degassed water and connected through inlet/outlet ports to a
140 circulation system for cooling. The rear part of the coupler is a cylindrical cavity for placing the
141 transducer, before the coupler is sealed by a lid and a silicone ring upon mechanical tightening.

142 To examine whether the focused sound field in the device meets the design expectations, we
143 conducted multiphysics simulations using COMSOL. For simplicity, a two-dimensional model was used
144 (see **Methods** for details). The calculated sound pressure field, sound pressure level field
145 (**Supplementary Fig. 1c**), and sound intensity field (**Fig. 1f**) were normalized and plotted as heat maps.
146 These results showed that the ultrasound waves converged along the expected two-dimensional cone to
147 reach the focal point. Subsequently, they reached the ExAW along the ideal reflection angle and were
148 absorbed by the sound-absorbing material (modeled as a perfect matching layer in the simulation).
149 These results clearly indicate a focal ultrasound stimulation at the target region of the cell culture area,
150 with significantly lower level of ultrasound outside of the focal region. Similar results can be observed
151 in the sound intensity field image as well. Such focused stimulation performance meets the goal of our
152 device design. To evaluate the importance of sound-absorbing materials, we attempted to remove it in
153 the simulation (**Supplementary Fig. 1d**) and then observed highly disordered, non-focal sound pressure
154 field and sound pressure level field in the device (**Supplementary Fig. 1e**), as illustrated by sound

155 waves undergoing multiple reflections. Under such condition, the energy cannot be accumulated at the
156 focal point, and a stable energy distribution cannot be calculated in the steady-state sound intensity field.
157 Therefore, the sound-absorbing material in the design of ECCD is crucial for ensuring a stable and
158 predictable focused sound field.
159

160 **An experimental platform for FUS stimulation and live-cell imaging based on ECCD**

161 In order to integrate ECCD with laser confocal microscopy, a carrier system was designed. This
162 system allows the transducer, coupler, and culture device to move freely in three dimensions within the
163 microscope's field of view, facilitating optical focusing and field-of-view selection. To this end, a three-
164 axis displacement platform, referred to as the primary displacement system, was employed (**Fig. 2a&b**).
165 This system also mechanically isolates the weight of the ultrasound transducer, coupler, and culture
166 device, from the microscope platform, thereby ensuring minimal disturbance to the optical systems as
167 well as universal applicability to different kinds of optical setups. Furthermore, ensuring alignment and
168 close contact between the ultrasound transducer coupler and the culture device is crucial for maintaining
169 the stability and predictability of the acoustic pathway during experiments. Therefore, a secondary
170 displacement system was mounted on the primary platform to control the relative motion between the
171 coupler and the culture device. This system, with only one degree of freedom in the vertical direction
172 (Z-axis), independently controls the vertical motion and applies additional load to achieve precise
173 alignment between the coupler and the EnAW. With such a two-level carrier system, independent
174 adjustments can be made to the acoustic pathway as well as the optical path relative to the microscope,
175 decoupling the control of ultrasound stimulation and that of microscopic imaging.

176 High-precision 3D printing was chosen to manufacture the coupler and ECCD. The ECCD was
177 made from MED610 photopolymer resin, which is commonly used in orthopedic and oral surgery[36] and
178 expected to exhibit good biocompatibility, thermal stability, and chemical stability under cell culture and

ultrasound stimulation conditions. It also demonstrates mechanical stability to prevent deformation, breakage, fatigue, and creep during assembly and experiments. The coupler was made from ABS photopolymer resin (acrylonitrile-butadiene-styrene copolymer) using high-precision 3D printing (**Fig. 2c&d**), due to the robustness, density, and stability of the materials.

For the acoustic windows mounted on the ECCD and the coupler, 1mm-thick acoustically transparent material was used to both ensure seamless coupling and avoid window bending due to liquid pressure under working conditions. These acoustic windows should be made from materials that do not significantly reflect sound waves at its interface with the culture medium (considered as water). Firstly, several common laboratory materials were tested for acoustic impedance, from which polydimethylsiloxane (PDMS) was found to have an impedance value close to that of water (**Fig. 2e&f**). Subsequently, different PDMS were tested, and the acoustic impedance of PDMS slab at 4:1 mixing ratio was found closest to that of water at the same temperature. Therefore, PDMS with base: curing agent ratios at 4:1 was used for making acoustic windows. Before conducting experiments, the primary displacement platform carrying the ultrasound stimulation system and the secondary displacement platform carrying the ECCD (**Fig. 2g**) are assembled and mounted on the optical table of the microscope (**Fig. 2h**).

In addition, we calibrated the acoustic field generated by the FUS transducer used in this study. In particular, the calibration was conducted using a hydrophone to measure the sound intensity field near the focal plane of the transducer. The results showed that when the input voltage to the transducer was 20 V, the frequency 1 MHz, the repetition frequency 10 kHz, and the duty cycle 30% for burst waves, the -3 dB focal region (where the sound intensity dropped to 50% of the maximum intensity) on the X-Y plane (perpendicular to the axis of the focusing acoustic cone) was approximately a circular area with a

201 diameter of 3 mm; while on the X-Z plane, the -3 dB focal region was an elliptical shape with a major
202 axis of about 18 mm and a minor axis of about 3 mm (**Supplementary Fig. 2a**).
203 Given that thermal effect due to HIFU is inevitable during experiments, we studied the dynamics
204 of average temperature change at the focal region. Specifically, we used a high-speed thermistor
205 measurement method. Specifically, a T25 culture bottle with a thermistor attached to the bottom and
206 filled with water was placed on the path of the FUS (**Supplementary Fig. 2b**). To ensure high thermal
207 sensitivity and minimal scattering of the acoustic waves, the thermistor was made from a platinum wire
208 (50 μm in diameter). To measure the average temperature over the focal region, the platinum wire was
209 bent and attached to a 3×3 mm^2 square area matching the size of the focal region (**Supplementary Fig.**
210 **2c-e**). Our results showed that under FUS stimulation, the temperature at the focal region could rise and
211 reach a steady state within about 5 s, and drop to the environmental temperature within 3 s after the FUS
212 was stopped, thus demonstrating the rapid temperature response at the focal region. Moreover, the target
213 temperature of the focal region can also be modulated by varying the ultrasound intensity and the duty
214 cycle of burst waves (**Supplementary Fig. 2f&g**).
215

216 **HIFU-induced cell ablation does not show significant correlation with ultrasound-caused**
217 **thermal effect**

218 To mimic the interaction between FUS and tissues (especially epithelial tissues, which are
219 commonly involved in ultrasound therapy), this study selected epithelial monolayer of Madin-Daby
220 canine kidney cells (MDCK cells) as an in vitro model. Firstly, to validate the compatibility of ECCD
221 with cell culture, MDCK cells were plated in ECCD and regular 60 mm culture dish and cultured for 2
222 days. At 50% and 100% confluence, no significant difference was observed between above two groups
223 in cell proliferation and epithelial colony morphology (**Fig. 3a**). In order to observe the shape and size of
224 focal region produced by FUS on MDCK monolayer in ECCD, we next set to simultaneously investigate

225 the temperature change of focal region and cell ablation under FUS stimulation. Although
226 abovementioned results from thermistor experiment showed the dynamics of average temperature
227 change in the focal region, it was not suitable for measuring the temperature field distribution of the
228 focal area. To characterize the temperature field, custom-made thermochromic tapes were used. These
229 tapes contained thermochromic inks with pre-calibrated color-changing temperatures of 31, 38, 45, and
230 65°C in red, yellow, green, and purple, respectively, and were mixed at volume ratio of 4:2:2:1. These
231 inks changed color from brick red at room temperature to green, blue, purple, and milky white at
232 temperatures of 34, 38, 43, and 62°C, respectively (**Fig. 3b**). These tapes were applied to the bottom of
233 the culture device before FUS experiments, and the color changes were recorded to reconstruct the
234 temperature field changes during ultrasound stimulation. Additionally, to detect cell ablation after
235 ultrasound stimulation, Live dye was used to label the entire monolayer of MDCK cells at 100%
236 confluence before the experiment.

237 Given that HIFU-based thermal effects are widely believed to be associated with ultrasound-
238 induced cell ablation in previous studies[4, 27], we next compared the changes in the focal region
239 temperature with the distribution of cell ablation. The "temperature field" was henceforth defined based
240 on the images of the thermochromic tape, with particular attention to the region where color change (*i.e.*,
241 temperature change) occurred. This temperature field could clearly visualize the focal area under FUS
242 treatment. Correspondingly, the images of cells captured under FITC fluorescence were henceforth
243 defined as the "cell field". Specifically, we define areas where cells were ablated (shown by the
244 disappearance of fluorescence during FUS treatment) as the "cell ablation area", and an elliptical-like
245 enveloping area that encloses all cell ablation area was defined as the focal area of cell field. Our results
246 indicated that under FUS stimulation, the focal area of the temperature field reached a steady state
247 within a short time (1-10 s). After stopping ultrasound, the focal area of the temperature field also

248 returned to ambient temperature within a relatively short time (**Supplementary Fig. 3a**). This was
249 consistent with the temperature change dynamics measured by thermistor-based method
250 (**Supplementary Fig. 2f&g**).

251 Of note, our results showed that the contours of the temperature field and the cell field were
252 roughly elliptical, with the major axis direction along the direction of ultrasound propagation (**Fig.**
253 **3c&d**). By measuring the lengths of the major and minor axes of the elliptical outline of the focal region
254 of the temperature field and cell field (**Fig. 3e**), we observed a positive correlation between FUS
255 intensity and the size of focal region of the temperature field, as well as that of the cell field. As
256 expected, similar correlation was also observed between FUS treatment time and above focal regions
257 (**Fig. 3c&d**).

258 However, by comparing the cell ablation area with the focal area of the temperature field, it is
259 clear that the focal area of the temperature field showed continuously decreasing temperature from the
260 center to the periphery, while the distribution of the cell ablation area was not necessarily continuous or
261 following the temperature gradient. Notably, the cell ablation area was a hollow elliptical shape under
262 conditions of high ultrasound intensity (transducer voltage 50 V, exposure time 3 min), and it became a
263 circular elliptical band under conditions of lower ultrasound energy (transducer voltage 20 V, exposure
264 time 3min), with non-uniform cell ablation within it (transducer voltage 40 V). Further quantitative
265 comparative analysis revealed no significant correlation in terms of shape and size between the cell
266 ablation area and the focal region of the temperature field (**Fig. 3f&g**). These observations suggested that
267 although changes in the temperature field occurred as expected within the elliptical focal region, the
268 continuous changes in the temperature field and the non-continuous, non-uniform changes in the cell
269 ablation area were inconsistent with the conventional understanding of ultrasound-based thermal

270 ablation theory. This implies that mechanisms other than thermal effects might exist for cell ablation
271 under FUS.

272 To further demonstrate that the thermal effects within the FUS focal area were insufficient to
273 ablate cells within this region in the short experimental observation time of this study, we placed the
274 ECCD (with a monolayer of MDCK cells at over 90% confluence) into water baths at 65°C and 85°C,
275 respectively, for 5 minutes. Compared with the untreated group, the proportion of cell ablation caused
276 by short-term treatment was less than 10% in both 65°C and 85°C groups (**Supplementary Fig. 3b&c**).
277 This is significantly different from the proportion of the cell ablation area within the focal region of cell
278 field under FUS stimulation. These results indicated that cell ablation produced under FUS stimulation
279 in a short time and the associated thermal effects in the focal area were not significantly correlated.
280 Therefore, it is necessary to explore cell ablation mechanisms beyond thermal effects.

281

282 **HIFU-induced cell ablation is associated with cavitation bubbles**

283 To explore cell ablation mechanisms under FUS stimulation beyond aforementioned thermal
284 effects, we performed experiments using MDCK cells expressing red fluorescent protein in cell nuclei
285 (H2B-RFP), with Live dye to simultaneously reflect cell viability (**Fig. 4a**). Of note, seconds after the
286 initiation of FUS stimulation, a large number of bubbles appeared in the cell ablation area. These
287 bubbles were opaque under bright field, but are nearly transparent in fluorescence channel with only a
288 halo the edge (**Fig. 4b**). We attributed these bubbles to the cavitation effect of FUS.

289 To investigate the relationship between ultrasound-induced bubbles and cell ablation, time-lapse
290 microscopy was performed with Dead dye simultaneously monitor the distribution of cell death. We
291 found that FUS-induced bubbles were significantly correlated with the changes in cell death (*i.e.*, cell
292 ablation) domain in morphology and spatial distribution (**Fig. 4c**). As the bubble clusters expanded, the
293 originally continuous monolayer of cells eventually ruptured. In addition, by observing the movement of

294 bubble clusters, they also move in response to ultrasound stimulation (**Fig. 4d**). At macroscopic level,
295 these results reflected significant mechanical interactions between FUS-induced bubbles and cells at the
296 target region.

297 Notably, after cell ablation, a layer of dead cells remained attached (**Fig. 4e**). Bright-field
298 imaging results showed that while this layer of dead cells still appear to connect with the rest of the cell
299 monolayer, its morphology differed significantly from live cells. This suggests that cell ablation under
300 ultrasound may not result in the complete disappearance of cells and their substances but leaves behind a
301 post-ablation phantom layer (PAPL) composed of cellular remnants. Importantly, the connections
302 formed by the cytoskeleton in the phantom layer appear intact, maintaining connections to adjacent live
303 cell monolayer. Although such connections might hold the phantom layer in its original place, it was
304 also observed that after long-term FUS treatment, or at the location where large bubble clusters form, the
305 phantom layer could break away from the substrate (**Fig. 4f**). In this process, even part of the live cell
306 monolayer connected to the phantom layer could be peeled off the substrate. Therefore, abovementioned
307 results indicate a significant correlation between FUS-induced air bubbles and the cell ablation
308 potentially via mechanical interactions between them. This suggests that it is critical to investigate
309 deeper into the mechanical interactions between FUS-induced bubbles and cells. Additionally, the
310 formation of the PAPL in above FUS-induce tissue damage model might represent a previously
311 unappreciated opportunity to recapitulate the wound created by HIFU-based cell ablation.

312

313 **Mechanolysis induced by subcellular bubble formation**

314 Above experiments provided macroscopic level clues regarding a mechanical mechanism
315 underlying HIFU-induced cell ablation mediated by cavitation bubbles. To further explore the
316 correlation between bubble formation and cell ablation at the microscopic level, we observed cellular
317 responses during FUS treatment at single-cell resolution. Live dye was used to track cell viability in

318 real-time. Our results showed that, as ultrasound stimulation proceeded, a subcellular air bubble
319 suddenly appeared where cells are attached. As the bubble grew, the fluorescence intensity of the cell
320 associated with the bubble started to decrease until almost no fluorescence signal could be detected in
321 the whole cell (**Fig. 5a**). Quantitative analysis of the average fluorescence intensity after the appearance
322 of the bubble revealed a rapid decay within a few seconds, followed by a minimally detectable plateau
323 (**Fig. 5b**). These results suggest that as the bubble grows, the cell membrane was broken, leading to the
324 outflow of cellular content and eventually cell death. Statistical analysis indicated that the fluorescence
325 signal of the cell decreased from the level of live cells to the background level in an average time of
326 about 10 seconds after the appearance of the bubble, (**Fig. 5c**). Compared to classical processes like
327 apoptosis or necrosis, this is a remarkably rapid process, implying a different mechanism for cell
328 ablation through mechanical interaction between cells and FUS-induced subcellular bubbles.
329 To investigate the mechanism by which bubbles induce cell ablation, we first needed to
330 determine the relative positions of bubbles and cells. Thus, we performed optical sections and 3D
331 reconstruction of GFP-expressing MDCK cells during FUS treatment. Specifically, there were 10 optical
332 sections (X-Y planes) were acquired along the z-axis, with section spacing 11.29 μm, and the total
333 scanning height 101.62 μm. The lowest optical section was lower than the bottom surface of the cell
334 (where there is no fluorescence), and the top optical section was higher than the top surface of the cell
335 (where there is no fluorescence) to ensure that the 3D reconstruction included the signals across entire
336 thickness of the cell. 3D reconstructed images (**Fig. 5d**) showed that, before bubble formation, the green
337 fluorescence was uniformly distributed within the cell. As the bubble formed, a non-fluorescent circular
338 area appeared inside the cell (from X-Y cross-section). X-Z and Y-Z sections further revealed that the
339 bubble's formation created a low-fluorescence area between the cell's original position and the substrate
340 (coverslip), surrounded by the GFP fluorescence signal of the cell itself, reflecting the bubble might

341 push part of the cell away from the substrate upon its formation. This suggests that under ultrasound
342 treatment, subcellular air bubbles may originate between the cell and the substrate, exerting a repulsive
343 force on the cell.

344 To further confirm that abovementioned bubbles, whose appearance resulted in a low-
345 fluorescence region inside the cell, were indeed formed between the cell and the substrate undeath it, we
346 compared them with another type of bubbles that are known to be positioned above, instead of
347 underneath, the cell, and thus do not generate a repulsive effect. Specifically, our quantitative analysis
348 showed that bubbles that eventually caused cell ablation significantly reduced the fluorescence signal at
349 where they appear, even before the cells died (**Fig. 5e**). Continuing to track these bubbles, we observed
350 that, after ablating the cell at its original location, they continued to attach to the substrate, grow, and
351 reach the culture space above surrounding live cells. In this case, these bubbles were simply positioned
352 above, instead of intruding into, the cells below, and such bubbles did not significantly affect the
353 fluorescence signal from cells underneath (**Fig. 5e; Supplementary Fig. 4a**). The comparison of above
354 two situations suggests that bubbles causing cell ablation and those floating on the cell surface exhibit
355 significant differences in optical effects, with the latter lacking a repulsive effect on the cell. This further
356 supports our hypothesis that bubbles causing cell ablation originate between the cell and the substrate,
357 creating repulsive forces that might eventually rupture the cell.

358 To further substantiate above hypothesis, we investigated the relationship between subcellular
359 bubble formation and cell membrane deformation, we performed Z-stack imaging on MDCK cells that
360 only expressed membrane-GFP during FUS treatment (**Fig. 5f**). To confirm that bubbles only appeared
361 between the cell and the substrate, we scanned only the bottom half of the cell close to the substrate. The
362 scanning height was 16.60 μm, consisting of 5 layers with a spacing of 4.15 μm. Under this setting, the
363 uppermost optical section was at the middle of the cell, and the lowest was below the cell membrane,

364 thus could capture the formation and growth of the bubble along with cell membrane deformation once
365 the bubble formed between the cell and the substrate. Our result showed that a bubble appeared at 7.6 s
366 after FUS treatment, and the membrane-GFP signal enveloping the bubble was also clearly observed
367 (**Fig. 5f**), suggesting that the bubble indeed formed between the cell and the substrate and caused close
368 contact with cell membrane. As the bubble gradually expanded, the membrane-GFP signal enveloping it
369 also expanded, reflecting the direct mechanical repulsive effect of the bubble on the cell membrane.
370 Importantly, at 38 s, the membrane-GFP signal enveloping the bubble no longer exhibited a continuous
371 curved shape but instead showed structures resembling bifurcated cracks, followed by cell rupture. This
372 provided direct experimental evidence that bubble formation and growth caused the expansion and
373 ultimate rupture of the cell membrane (**Fig. 5f**). Additionally, we observed that some bubbles
374 disappeared on their own after formation, and with time, the fluorescence signal of the live cells in their
375 occupied area gradually recovered. This further supports the repulsive effect caused by bubble to the cell
376 (**Fig. 5g**).

377 Altogether, while we do not rule out the possibility that thermal effects by FUS may contribute
378 to the ablation of some cells within the focal zone, the above results suggest that the formation of
379 subcellular bubbles between the cell and the substrate and their repulsive effect on the cell impose
380 significant mechanical loads on the cell membrane, leading to continuous expansion and eventual
381 rupture. This process is distinct from classical mechanisms of ultrasound-induced cell ablation and
382 represents a previously unappreciated mechanism, which we termed ultrasound-inflicted “mechanolysis".

383 Furthermore, whether bubbles exert mechanical effects on the cell nucleus is another important
384 question. Therefore, we conducted FUS stimulation experiments on MDCK cells expressing H2B-RFP,
385 simultaneously using Live dye to monitor cell viability. The results showed that bubbles generally did
386 not form directly beneath the cell nucleus (**Supplementary Fig. 4b**), and the morphology of the cell

387 nuclei in the PAPL did not show significant distortions after cell ablation, suggesting less significant
388 effect of subcellular bubbles on cell nucleus than that on the cell membrane. In some cells, it was indeed
389 observed that when the formation of a bubble occurred near the cell nucleus, it could cause mechanical
390 compression and deformation of the cell nucleus, but not to a degree significant enough to induce
391 notable translocation or rupture of the cell nucleus (**Supplementary Fig. 4c**). This suggests that the
392 mechanical effect of bubbles on the cell membrane may be a critical factor in FUS-inflicted
393 mechanolysis

394 Therefore, based on above findings, the interactions between HIFU-induced bubbles and the cell
395 could be largely grouped into three different types (**Fig. 5h**). When bubbles form between the cell and
396 the substrate, if they may persist for a short time before disappearing, the cell could gradually refill the
397 void space created by the bubble. For bubbles that form and consistently grow between the substate and
398 the cell, they can cause significant deformation of the cell membrane, ultimately leading to
399 mechanolysis of the cell. Finally, as these bubbles further enlarge, they may eventually penetrate
400 through the PAPL and detach from the substrate.

401

402 **Collective cell migration and wound healing after HIFU-induced cell ablation**

403 The wound healing response after ultrasound-induced cell ablation holds significant practical
404 implications, yet there is a lack of exploration in previous studies. Using only mechanical scratch or
405 place-holders to create empty space that cells could migrate into does not recapitulate key features of
406 ultrasound-inflicted wounding, such as the residue of cell/tissue debris left at the original place after
407 ultrasound ablation, thereby limiting their applications in understanding subsequent wound healing
408 response. In this study, the HIFU-induced ablation successfully created a unique type of wound, termed
409 the PAPL, within a continuous epithelial monolayer, providing a more biomimetic model of HIFU-

410 inflicted wounding. Herein we apply this model to study the collective cell migration and wound healing
411 after HIFU-induced ablation.

412 To this end, we continued to culture cells in ECCD after HIFU ablation and tracked the
413 migration of the cells close to the wounded PAPL area (**Fig. 6**). Under experimental conditions that
414 allow the PAPL to remain entirely or partially attached to the substrate after ablation, we explored how
415 it might regulate the collective migration of the neighboring live cells and the closure of the wound.
416 Using H2B-mCherry MDCK cell monolayers, we found that live cells actively and directionally
417 extended and migrated towards the area where the PAPL remained after ablation until the ultrasound-
418 inflicted wound was completely closed. During this process, there remained a connection between the
419 PAPL and live cells, and live cells also reconstructed the PAPL during the closure of the wound.
420 Additionally, under conditions where ultrasound was strong enough to cause the detachment of the
421 PAPL, we observed that live cells around the wound area could still migrate into the clear area left at the
422 original place of the PAPL. This indicates that cells are intrinsically able to migrate towards the wound
423 area regardless of the presence of the PAPL. Importantly, during the process of collective cell migration
424 and wound healing, we observed a phenomenon of "fracture" between some "leading cells" at the
425 migration front and the cells behind them, forming new tissue gaps. This implies a process of secondary
426 damage that is generated spontaneously during the repair of the primary wound inflicted by ultrasound
427 ablation) (**Fig. 6b**). This may be due to the different directions and speeds of movement of cells within
428 the cell monolayer nearby the wound. Such secondary damages were often repaired again after the
429 closure of the primary ultrasound-induced wound.

430 To further investigate the influence of the PAPL on the dynamics of collective cell migration and
431 wound healing response after ultrasound ablation, we selected cases where part of the PAPL remained
432 attached to the substrate, and tracked and analyzed the cell migration nearby. As shown in **Fig. 7a**, the

433 live cell monolayer in this case could migrate into both the PAPL and the free area (where the PAPL had
434 detached but still available for live cells to migrate into), providing a basis for analyzing and comparing
435 the differential guiding effect imposed by the PAPL and the free area on cell migration. As shown in **Fig.**
436 **7b**, by tracking cell migration trajectories, we found that although the initial migration direction was
437 relatively uniform, it was significantly influenced by the PAPL and changed direction gradually,
438 preferentially migrating into the area where the PAPL remained. By calculating the angle θn
439 (counterclockwise) between the migration direction of each cell and the horizontal direction of the
440 viewport, and comparing it with the orientation angle of the interface between the PAPL and the free
441 area (θ_1 and θ_2 in **Fig. 7b**), we found that as the wound healing proceeded, the difference between θ_n and
442 θ_1 or θ_2 decreased (**Fig. 7c**). In the meantime, analysis of cell movement revealed an average speed of
443 18-43.2 μm/h during the collective cell migration and wound healing process (**Fig. 7d**). Above results
444 indicates that the cell migration direction gradually turned towards the PAPL, and away from the clear
445 area, in a manner approximately aligned with the interface between the PAPL and the free area. These
446 results suggest that the PAPL, although no longer possessing live-cell activity, still exhibits biological
447 activity and can interact with neighboring cells to regulate their movement. This is different from the
448 traditional free-boundary wound healing process and indicates a previously underexplored mechanism
449 that might play an important role in dictating collective cell migration and wound healing after HIFU-
450 induced ablation. Such mechanism poses an interesting question worthy of future studies.
451

452 **DISCUSSION**

453 In this study, we designed and built an enclosed cell culture device capable of simultaneously
454 achieving non-invasive ultrasound stimulation and long-term online live-cell imaging. Additionally, we
455 established an in vitro platform to explore the biological effects of ultrasound. In comparison to previous
456 experimental methods, this platform offers several advantages. First, it can achieve controllable FUS

457 stimulation and ablation of cells within a pre-defined target region, while cells outside the focal area
458 could remain live, thus providing a technical basis for investigating changes between cells subject to
459 different levels of ultrasonic stimulation in the same culture environment. Secondly, this platform is
460 compatible with long-term cell culture and real-time microscopic imaging. By avoiding the cell
461 contamination risks associated with previous methods, this platform allows the study of both the passive
462 response of cells to short-term FUS stimulation and the continuous observation of the active post-
463 stimulation response of cells over an extended period. This provides an essential technical basis for
464 studying long-term biological effects and response following ultrasound treatment.

465 This study provided direct experimental evidence for HIFU-inflicted mechanolysis, which is a
466 previously unreported biomechanical mechanism of ultrasound-induced cell ablation. In earlier studies,
467 it has been reported that ultrasound might induce cell damage due to the cavitation effect, or by
468 mechanical disruption of cells in suspension[33, 37, 38]. However, the mechanical mechanisms of
469 ultrasound-based ablation remain underexplored, with limited direct experimental evidence. By far,
470 there are several hypotheses. Firstly, the microflow around the oscillating bubble near the cell might
471 impose large shear force to the cell membrane to produce repairable, reversible perforation[30, 39, 40].
472 Secondly, under inertial cavitation, when the pressure of the bubble is higher than a certain threshold,
473 the bubble will implode and release a shock wave that can damage the cell membrane and perforate the
474 cell membrane[41, 42]. Thirdly, under inertial cavitation, the non-spherical collapse of the bubble near the
475 rigid boundary might produce a liquid jet with high pressure[43], which can lead to permanent damage of
476 the membrane and detachment of the cell from the substrate[44]. In our study, we found that the cavitation
477 bubbles produced under HIFU can also cause mechanolysis of cells without collapsing. In such scenario,
478 because the bubble did not collapse during the process of cell ablation and had a significant volume
479 growth instead, it was evidently different from abovementioned three mechanistic hypotheses proposed

480 by previous studies. Therefore, the mechanolysis mechanism mediated by the formation and growth of
481 ultrasonic cavitation bubbles discovered in this study provide a previously unappreciated mechanism,
482 which may provide theoretical guidance for innovative development of the applications of FUS in the
483 future.

484 The experimental platform developed in this study also provides a foundation for exploring long-
485 term biological responses following ultrasound stimulation, such as wound healing responses after
486 HIFU-induced ablation. Wound healing is a significant research topic in the field of medicine. For
487 studying the wound healing process, in vitro models, due to their more controllable environment
488 compared to in vivo models, are widely adopted for investigating wound healing mechanisms. Currently,
489 commonly used in vitro wound healing models are based on mechanical scratches or pre-occupied void
490 area[45, 46] to create free spaces for cells to migrate into. In addition to scratching, various methods such as
491 stamping, thermal stimulation, electric shocks, and laser illumination have been employed in monolayer
492 cell cultures to create "wounds"[47-50]. However, these models remain difficult to recapitulate the tissue
493 damage inflicted by ultrasound ablation, thereby hindering the understanding of the wound healing
494 process post-ultrasound treatment and limiting insights into the factors regulating the collective cell
495 migration during such wound healing. In this study, we achieved FUS ablation in a monolayer of cells in
496 vitro and observed a residual layer of cell remnants (the PAPL) left at the site of the ablation, providing
497 a unique model and method for understanding and studying the collective cell migration and wound
498 healing response after ultrasound treatment. Compared to traditional models of free-edge cell migration,
499 our model provides a more biomimetic representation of the ultrasound-inflicted wound. The
500 interactions between the PAPL and neighboring live cells further demonstrate its biological activity and
501 effects that can guide the direction of collective cell migration, a phenomenon not reported in previous
502 studies. Regarding such correlation between the PAPL and collective cell migration in wound healing,

503 we speculate that it might be related to intercellular connections between live cells and the PAPL.
504 Additionally, the release of lysophosphatidic acid during cell lysis and its activation of various
505 downstream signals might also contribute to this phenomenon[51, 52]. The specific mechanisms behind this
506 phenomenon await further exploration. In the future, this wound healing model might be used to explore
507 the therapeutic effects of FUS-based tumor ablation and the subsequent wound healing process in
508 adjacent normal tissues. Based on findings reported in this study, there might be more biomechanical
509 regulatory mechanisms and related application to be explored regarding the post-ablation wound healing
510 process.

511 In summary, the ECCD developed in this study integrates non-invasive ultrasound stimulation
512 and long-term live-cell imaging, providing a unique technological platform for in-depth exploration of
513 the mechanisms underlying ultrasound-induced biological effects. Based on this, we discovered
514 mechanism of ultrasound ablation via cavitation bubble formation and growth-mediated mechanolysis of
515 cells, adding another layer of our understanding of the biomechanical principles of ultrasound therapy.
516 The post-ablation wound healing model feature a PAPL layer and its interaction with collective cell
517 migration also offer new perspectives and methods for investigating tissue wound healing mechanisms.
518 The findings of this study might contribute to broaden our understanding of the biological effects of
519 ultrasound, and inspire advancements in the applications for FUS-based therapy.

520

521 **ACKNOWLEDGEMENTS**

522 We thank Dr. Haidong Wang for assistance in thermistor measurement. We thank Dr. Jiabin Zhang and
523 Dr. Feng Feng for assistance in ultrasound transducer calibration. We thank Dr. Yan Yi for the gift of
524 the ultrasound-absorbent rubber. We thank Dr. Jianbo Bai for the gift of the H2B-RFP MDCK cell line.
525 Y.S.'s work is supported by the National Natural Science Foundation of China (U21A20203, 12102229),
526 the National Key Research and Development Program of China (2021YFA0719301), the Oversea High-

level Scholar Introduction Program, Tsinghua University Dushi Program, and the Tsinghua University Startup Funding.

AUTHOR CONTRIBUTIONS

Z.B. and Y.S. conceived the project; Z.B. designed and performed experiments; Z.B., Z.L., and Y.S. analyzed data. Y.S. supervised the project. All authors contributed to the manuscript.

COMPETING FINANCIAL INTERESTS

The authors declare no competing financial interest.

537 **REFERENCES**

538 1. Krishna V, Sammartino F, Rezai A. A Review of the Current Therapies, Challenges, and Future
539 Directions of Transcranial Focused Ultrasound Technology: Advances in Diagnosis and
540 Treatment. *JAMA Neurol* **75**, 246-254 (2018).

541 2. Izadifar, Izadifar, Chapman, et al. An Introduction to High Intensity Focused Ultrasound:
542 Systematic Review on Principles, Devices, and Clinical Applications. *J. Clin. Med.* **9**, 460 (2020).

543 3. Meng, Y., Hynynen, et al. Applications of focused ultrasound in the brain: from thermoablation
544 to drug delivery. *Nat. Rev. Neurol.* **17**, 7-22 (2021).

545 4. Recker, F., Thudium, et al. Multidisciplinary management to optimize outcome of ultrasound-
546 guided high-intensity focused ultrasound (HIFU) in patients with uterine fibroids. *Sci. Rep.* **11**,
547 22768 (2021).

548 5. Yu Tang, Chun Chen, Binglei Jiang, et al. Bifidobacterium bifidum-Mediated Specific Delivery
549 of Nanoparticles for Tumor Therapy. *Int. J. Nanomed.* **16**, 4643-4659 (2021).

550 6. Lipsman, N., Meng, et al. Blood–brain barrier opening in Alzheimer's disease using MR-guided
551 focused ultrasound. *Nat. Commun.* **9**, 2336 (2018).

552 7. Shashank R. Sirsi, Mark A. Borden. State-of-the-art materials for ultrasound-triggered drug
553 delivery. *Adv. Drug Delivery Rev.* **72**, 3-14 (2014).

554 8. Kelsie F Timbie, Umara Afzal, Abhijit Date, et al. MR image-guided delivery of cisplatin-loaded
555 brain-penetrating nanoparticles to invasive glioma with focused ultrasound. *J. Controlled*
556 *Release* **263**, 120-131 (2017).

557 9. Saira Alli, Carlyn A. Figueiredo, Brian Golbourn, et al. Brainstem blood brain barrier disruption
558 using focused ultrasound: A demonstration of feasibility and enhanced doxorubicin delivery. *J.*
559 *Controlled Release* **281**, 29-41 (2018).

560 10. Cao Y, Chen Y, Yu T, et al. Drug Release from Phase-Changeable Nanodroplets Triggered by
561 Low-Intensity Focused Ultrasound. *Theranostics* **8**, 1327-1339 (2018).
562 11. Matos, Maria B. C. De, et al. Ultrasound-Sensitive Liposomes for Triggered Macromolecular
563 Drug Delivery: Formulation and In Vitro Characterization. *Frontiers in Pharmacology*, 10
564 (2019).
565 12. Ying Meng et al. MR-guided focused ultrasound enhances delivery of trastuzumab to Her2-
566 positive brain metastases. *Sci. Transl. Med.* **13**, 4011 (2021).
567 13. Stavarache, M. A., Petersen, N., et al. Safe and stable noninvasive focal gene delivery to the
568 mammalian brain following focused ultrasound. *J. Neurosurg.* **130**, 989-998 (2019).
569 14. Nickolai Sheikov, Nathan McDannold, Natalia Vykhodtseva, et al. Cellular mechanisms of the
570 blood-brain barrier opening induced by ultrasound in presence of microbubbles. *Ultrasound in*
571 *Medicine & Biology* **30**, 979-989 (2004).
572 15. Chen H, Konofagou EE. The Size of Blood–Brain Barrier Opening Induced by Focused
573 Ultrasound is Dictated by the Acoustic Pressure. *J. Cereb. Blood Flow Metab.* **34**, 1197-1204
574 (2014).
575 16. Colleen T. Curley et al. Augmentation of brain tumor interstitial flow via focused ultrasound
576 promotes brain-penetrating nanoparticle dispersion and transfection. *Sci. Adv.* **6**, 1344 (2020).
577 17. Miguel N. Centelles, Michael Wright, Po-Wah So, et al. Image-guided thermosensitive
578 liposomes for focused ultrasound drug delivery: Using NIRF-labelled lipids and topotecan to
579 visualise the effects of hyperthermia in tumours. *J. Controlled Release* **280**, 87-98 (2018).
580 18. Paul Cressey, Maral Amrahli, Po-Wah So, et al. Image-guided thermosensitive liposomes for
581 focused ultrasound enhanced co-delivery of carboplatin and SN-38 against triple negative breast
582 cancer in mice. *Biomaterials* **271**, 120758(2021).

583 19. Patricia C. Rinaldi, Joie P. Jones, Frederick Reines, et al. Modification by focused ultrasound
584 pulses of electrically evoked responses from an in vitro hippocampal preparation. *Brain Res.* **558**,
585 36-42 (1991).
586 20. Po-Hsiang Tsui, Shyh-Hau Wang, Chih-Chung Huang. In vitro effects of ultrasound with
587 different energies on the conduction properties of neural tissue. *Ultrasonics* **43**, 560-565 (2005).
588 21. David P. Darrow, Parker O'Brien, Thomas J. Richner, et al. Reversible neuroinhibition by
589 focused ultrasound is mediated by a thermal mechanism. *Brain Res.* **12**, 1439-1447 (2019).
590 22. T. Zhang et al. Transcranial Focused Ultrasound Stimulation of Periaqueductal Gray for
591 Analgesia. *IEEE Trans. Biomed. Eng.* **69**, 3155-3162 (2022).
592 23. Cotero, V., Graf, et al. Stimulation of the hepatoportal nerve plexus with focused ultrasound
593 restores glucose homoeostasis in diabetic mice, rats and swine. *Nat. Biomed. Eng.* **6**, 683–705
594 (2022).
595 24. Yixin Zhong, Yu Zhang, Jie Xu, et al. Low-Intensity Focused Ultrasound-Responsive Phase-
596 Transitional Nanoparticles for Thrombolysis without Vascular Damage: A Synergistic
597 Nonpharmaceutical Strategy. *ACS Nano* **13**, 3387-3403 (2019).
598 25. Zachs, D.P., Offutt, et al. Noninvasive ultrasound stimulation of the spleen to treat inflammatory
599 arthritis. *Nat. Commun.* **10**, 951 (2019).
600 26. Huerta, T.S., Devarajan, et al. Targeted peripheral focused ultrasound stimulation attenuates
601 obesity-induced metabolic and inflammatory dysfunctions. *Sci. Rep.* **11**, 5083 (2021).
602 27. Kennedy, J. High-intensity focused ultrasound in the treatment of solid tumours. *Nat. Rev.*
603 *Cancer* **5**, 321–327 (2005).
604 28. Kok H P, Cressman E N K, Ceelen W, et al. Heating technology for malignant tumors: A review.
605 *Int. J. Hyperthermia* **37**, 711-741 (2020).

606 29. Hynynen, K., et al. A scanned, focused, multiple transducer ultrasonic system for localized
607 hyperthermia treatments. *Int. J. Hyperthermia* **3**, 21-35 (1987).
608 30. Junru Wu, Wesley L. Nyborg. Ultrasound, cavitation bubbles and their interaction with cells.
609 *Adv. Drug Delivery Rev.* **60**, 1103-1116 (2008).
610 31. Hu, Zhang, Unger, et al. Focused Ultrasound-Induced Cavitation Sensitizes Cancer Cells to
611 Radiation Therapy and Hyperthermia. *Cells* **9**, 2595 (2020).
612 32. Manabu Kinoshita, Kullervo Hynynen. A novel method for the intracellular delivery of siRNA
613 using microbubble-enhanced focused ultrasound. *Biochem. Biophys. Res. Commun.* **335**, 393-
614 399 (2005).
615 33. Robyn K. Schlicher, Harish Radhakrishna, Timothy P. Tolentino, et al. Apkarian, Vladimir
616 Zarnitsyn, Mark R. Prausnitz, Mechanism of intracellular delivery by acoustic cavitation.
617 *Ultrasound in Medicine & Biology* **32**, 915-924 (2006).
618 34. Qiu, Zhihai, et al. The Mechanosensitive Ion Channel Piezo1 Significantly Mediates In Vitro
619 Ultrasonic Stimulation of Neurons. *iScience* **21**, (2019).
620 35. Yao-Shen Huang, Ching-Hsiang Fan, Ning Hsu, et al. Sonogenetic Modulation of Cellular
621 Activities Using an Engineered Auditory-Sensing Protein. *Nano Lett.* **20**, 1089-1100 (2020).
622 36. Hideki Kitamori, Iori Sumida, Tomomi Tsujimoto, et al. Evaluation of mouthpiece fixation
623 devices for head and neck radiotherapy patients fabricated in PolyJet photopolymer by a 3D
624 printer. *Physica Medica* **58**, 90-98 (2019).
625 37. Douglas L. Miller, Alun R. William. Bubble cycling as the explanation of the promotion of
626 ultrasonic cavitation in a rotating tube exposure system. *Ultrasound in Medicine & Biology* **15**,
627 641-648 (1989).

628 38. Victor Frenkel, Eitan Kimmel, Yoni Iger. Ultrasound-induced intercellular space widening in
629 fish epidermis. *Ultrasound in Medicine & Biology* **26**, 473-480 (2000).
630 39. Hidemi Honda, Qing-Li Zhao, Takashi Kondo. Effects of dissolved gases and an echo contrast
631 agent on apoptosis induced by ultrasound and its mechanism via the mitochondria-caspase
632 pathway. *Ultrasound in Medicine & Biology* **28**, 673-682 (2002).
633 40. Alexander A. Doinikov, Ayache Bouakaz. Theoretical investigation of shear stress generated by
634 a contrast microbubble on the cell membrane as a mechanism for sonoporation. *J. Acoust. Soc.*
635 *Am.* **128**, 11–19 (2010).
636 41. Wrenn SP, Dicker SM, Small EF, et al. Bursting bubbles and bilayers. *Theranostics* **2**, 1140-
637 1159 (2012).
638 42. Lokhandwalla, M., Sturtevant, et al. Mechanical haemolysis in shock wave lithotripsy (swl): i.
639 analysis of cell deformation due to swl flow-fields. *Phys. Med. Biol.* **46**, 413-413 (2001).
640 43. E.A Brujan. The role of cavitation microjets in the therapeutic applications of ultrasound.
641 *Ultrasound in Medicine & Biology* **30**, 381-387 (2004).
642 44. Ohl, Claus-Dieter et al. Sonoporation from Jetting Cavitation Bubbles. *Biophys. J.* **91**, 4285–
643 4295 (2006).
644 45. Tao, H., Berno, et al. In vitro human keratinocyte migration rates are associated with SNPs in the
645 KRT1 interval. *PLoS One* **2**, 697 (2007).
646 46. Nadine B. Wolf, Sarah Küchler, Michal R. Radowski, et al. Influences of opioids and
647 nanoparticles on in vitro wound healing models. *Eur. J. Pharm. Biopharm.* **73**, 34-42 (2009).
648 47. Stamm, Anne, Reimers, et al. In vitro wound healing assays – state of the art. *BioNanoMaterials*
649 **17**, 79-87 (2016).

650 48. Kai Safferling, Thomas Sütterlin, Kathi Westphal, et al. Wound healing revised: A novel
651 reepithelialization mechanism revealed by in vitro and in silico models. *J. Cell Biol.* **25**, 691–709
652 (2013).
653 49. Van Kilsdonk, Jeroen WJ, et al. An in vitro wound healing model for evaluation of dermal
654 substitutes. *Wound Repair and Regeneration* **21**, 890-896 (2013).
655 50. Ud‐Din, Sara, Ardeshir Bayat. Non‐animal models of wound healing in cutaneous repair: In
656 silico, in vitro, ex vivo, and in vivo models of wounds and scars in human skin. *Wound Repair*
657 *and Regeneration* **25**, 164-176 (2017).
658 51. George Broughton, I. I., Jeffrey E. Janis, et al. The basic science of wound healing. *Plast.*
659 *Reconstr. Surg.* **117**, 12S-34S (2006).
660 52. Schreml, Stephan, et al. Wound healing in the 21st century. *J. Am. Acad. Dermatol.* **63**, 866-881
661 (2010).
662
663
664
665

666 **FIGURES and FIGURE CAPTIONS**

667 **Figure 1**

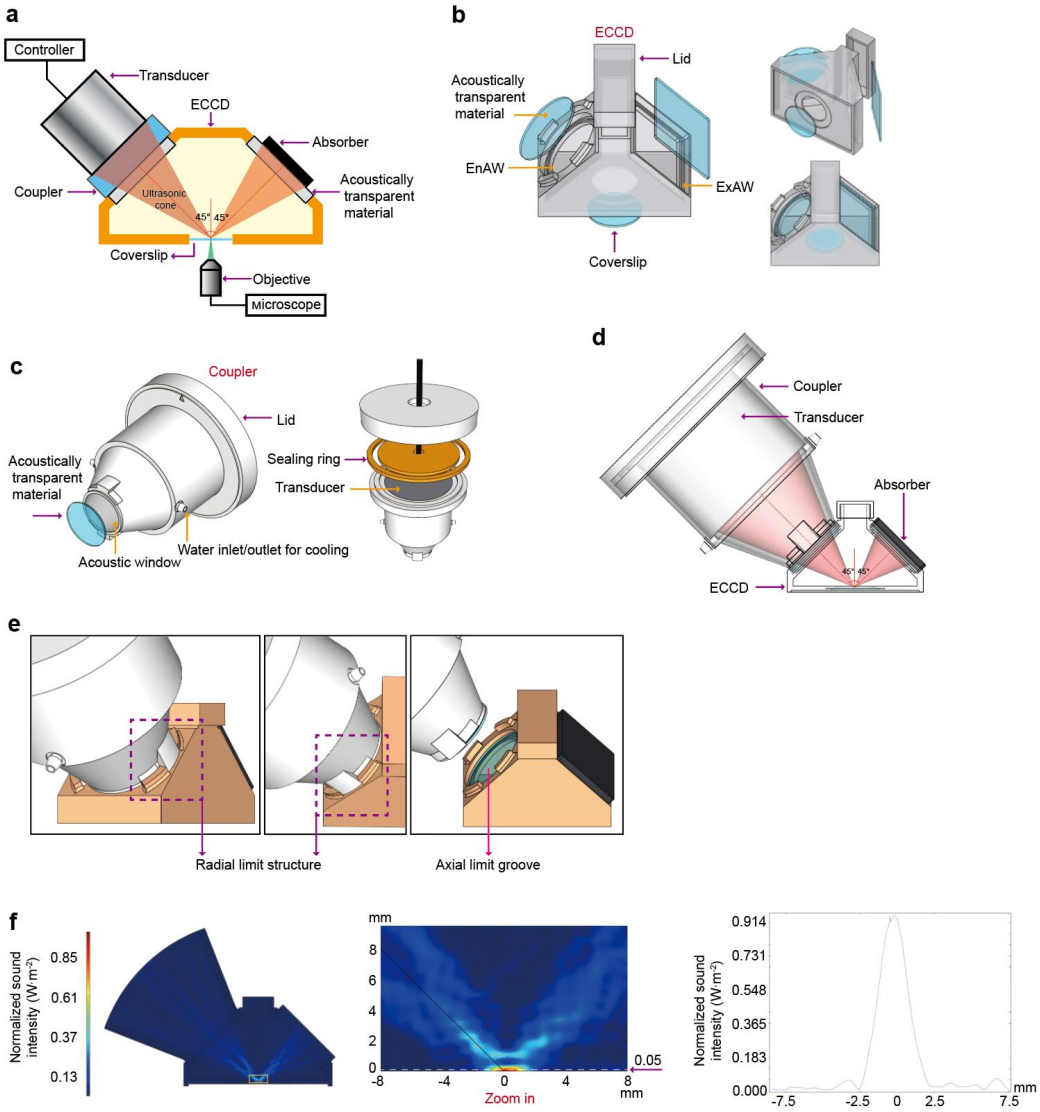

668

669 **Figure 1. Principle and design of the enclosed cell culture device compatible with focused**

670 **ultrasound stimulation and long-term microscopy imaging. (a)** Schematic diagram of the device

671 design and the acoustic pathway for focused ultrasound (FUS). **(b)** Structural design of the ECCD. **(c)**

672 Structural design of the FUS transducer coupler. **(d)** Schematic showing the assembly of the FUS

673 transducer and cell culture device with the acoustic pathway (schematic was drawn real component

674 proportions). **(e)** Design of the transducer coupler and positioning structure on the cell culture device. **(f)**

675 Computational results of the FUS acoustic field. Zoom-in displays the intensity field in the focal region.
676 The curve on the right shows the variation of intensity along the line drawn across the focal region, with
677 intensity represented by I_{sppa} (spatial peak pulsed average intensity, the maximum pulsed average
678 intensity on the acoustic field or a specified plane, in units of W/cm^2).
679

680 **Figure 2**

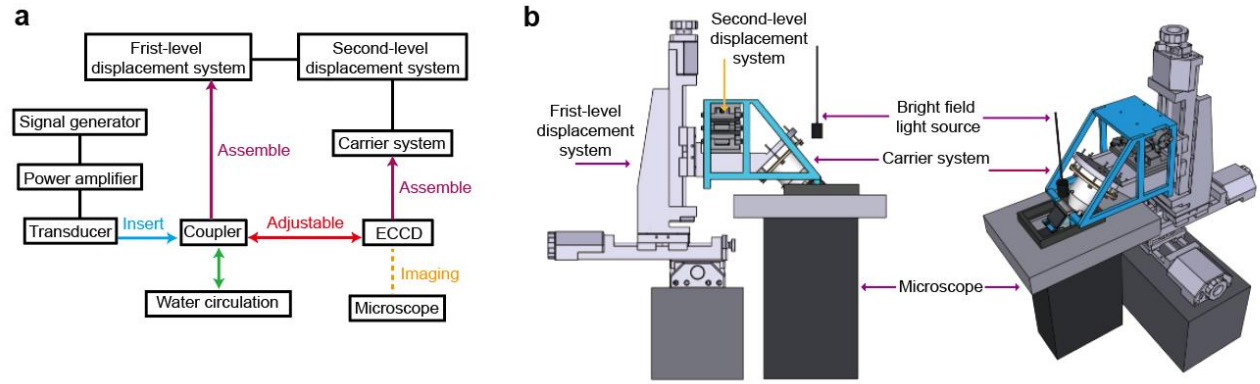

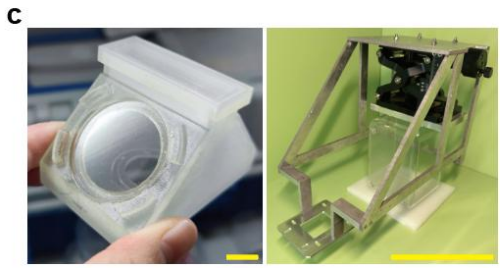

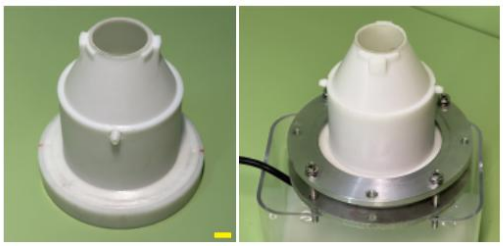

e

Materials	Sound velocity ($m \cdot s^{-1} \cdot 10^3$)	Density ($Kg \cdot m^{-3} \cdot 10^3$)	Acoustic impedance ($Kg \cdot m^{-2} \cdot s^{-1} \cdot 10^6$)
Plastic (T25 flask)	2.766	1.035	2.863
Plastic (35mm dish)	3.020	1.046	3.159
Silica gel	1.003	1.049	1.052
Acrylic plate	4.023	1.189	4.783
Plastic (culture plate)	2.753	1.044	2.874
MED610 light-cured resin	2.711	1.168	3.166
PDMS (4:1)	1.203	1.030	1.239
Pure water	1.500	1.000	1.500

f

Ratio of base to curing agent	Sound velocity ($m \cdot s^{-1} \cdot 10^3$)	Density ($Kg \cdot m^{-3} \cdot 10^3$)	Acoustic impedance ($Kg \cdot m^{-2} \cdot s^{-1} \cdot 10^6$)
10:1	1.058	1.034	1.094
5:1	1.123	1.031	1.157
4:1	1.203	1.030	1.239
3:1	1.115	1.029	1.148
2:1	1.059	1.025	1.085
1:1	1.052	1.024	1.077

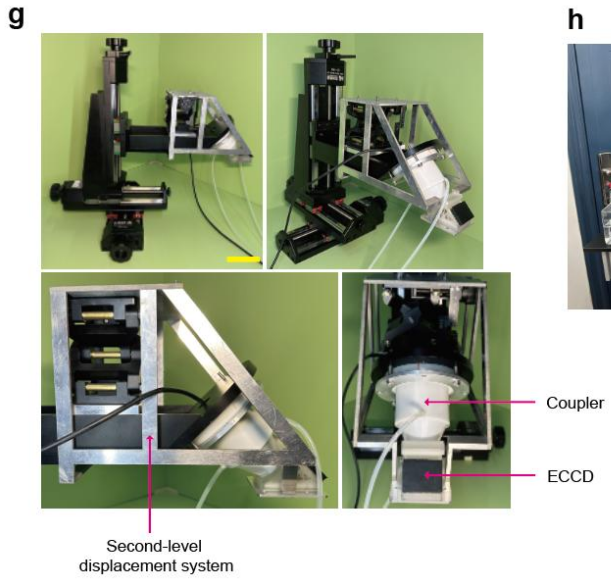

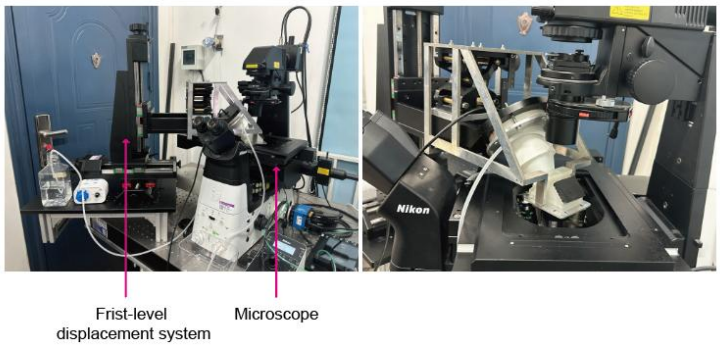

681

682 **Figure 2. Experimental setup for ultrasound stimulation and live-cell imaging based on the**
683 **ECCD.** **(a)** Flowchart showing the experimental setup and its operational procedure. **(b)** Design of the
684 primary and secondary displacement devices. **(c)** Photos of the ECCD and its tray system. The tray
685 system is connected to the displacement systems mentioned above. Scale bar: 10 mm. **(d)** Photos of the
686 FUS transducer coupler. Scale bar: 10 mm. **(e)** Selected acoustically transparent materials and their
687 measured acoustic parameters. Testing temperature: 25℃. **(f)** Table of acoustic parameters for PDMS
688 slab formed by mixing base liquid and curing agent in different proportions. Testing temperature: 25℃.
689 **(g)** Assembly of the displacement system, support system, ultrasound stimulation system, and cell
690 culture system. Scale bar: 10 cm. **(h)** Photos of the assembly of the ultrasound cell stimulation
691 experiment system and the microscope system.
692

Figure 3

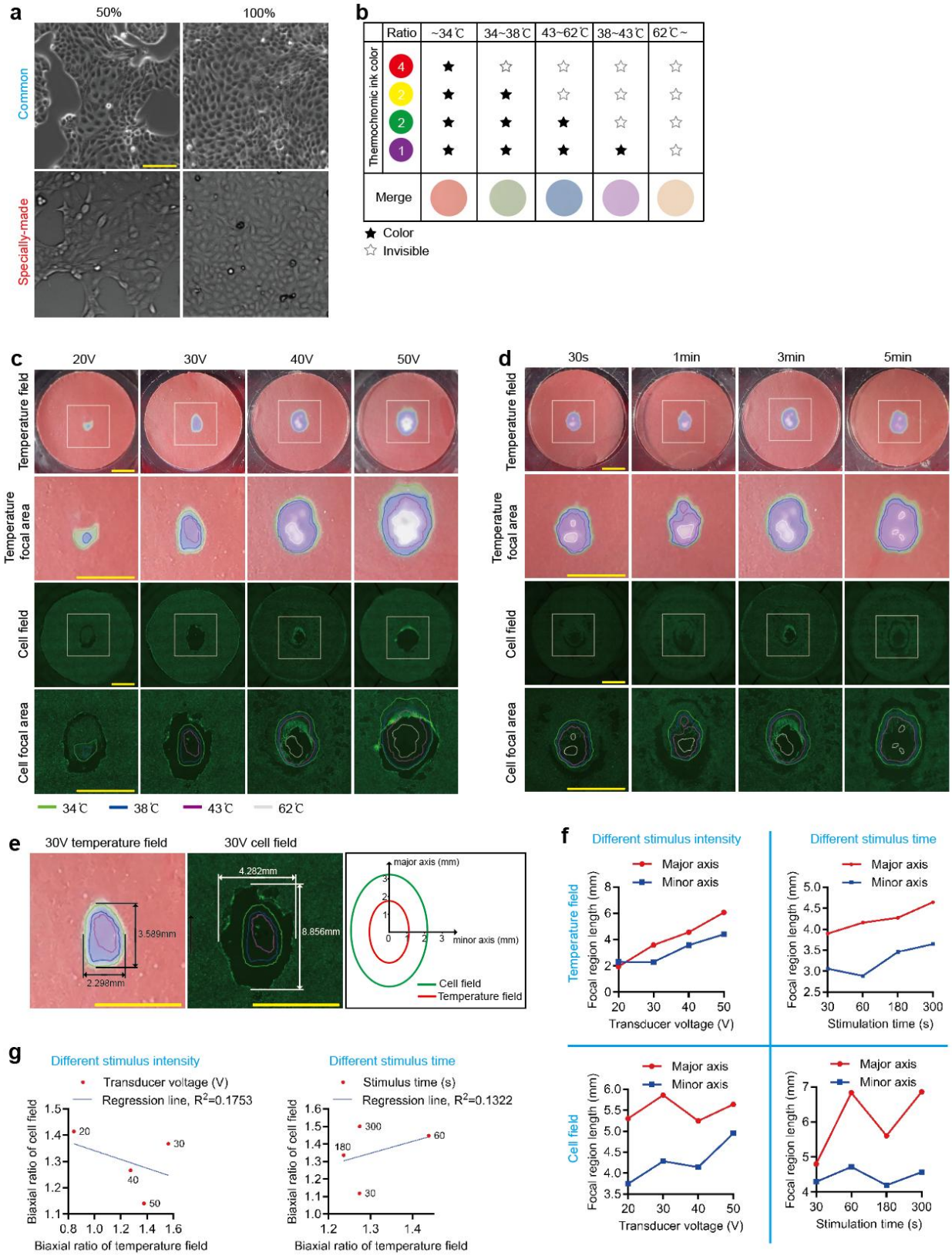
a
50%
100%
Common
Specially-made
b
Ratio
~34℃
34~38℃
43~62℃
38~43℃
62℃~
Thermochromic ink color
4
2
2
1
Merge
Color
Invisible
c
20V
30V
40V
50V
Temperature field
Temperature focal area
Cell field
Cell focal area
34℃
38℃
43℃
62℃
d
30s
1min
3min
5min
e
30V temperature field
30V cell field
3.589mm
2.298mm
4.282mm
8.856mm
major axis (mm)
minor axis (mm)
Cell field
Temperature field
f
Different stimulus intensity
Different stimulus time
Major axis
Minor axis
Temperature field
Cell field
Focal region length (mm)
Transducer voltage (V)
Stimulation time (s)
g
Different stimulus intensity
Different stimulus time
Transducer voltage (V)
Stimulus time (s)
Regression line, R2=0.1753
Regression line, R2=0.1322
Biaxial ratio of cell field
Biaxial ratio of temperature field

695 **Figure 3. HIFU-induced cell ablation does not show significant correlation with ultrasound-**
696 **caused thermal effect. (a)** Bright-field images of MDCK cells cultured in regular 35 mm culture dishes
697 and ECCD at confluence of 50% and 100%, respectively. Scale bar: 100 μm. **(b)** Table showing the
698 temperature-dependent coloration of the four-color thermochromic ink at different temperatures. The
699 mixing ratio is red: yellow: green: purple = 4:2:2:1. **(c)** The top row shows images of the
700 thermosensitive color-changing sticker attached to the ECCD bottom changing color at the focal point
701 under the influence of FUS. The FUS transducer emits continuous waves at a frequency of 1MHz with
702 indicated voltages for 3 min. The second row shows zoom-in images of the focal region. The third row
703 shows FITC fluorescence images at the focal point after the termination of FUS treatment. Live dye is
704 used on cells, and non-fluorescent regions reflect cell ablation areas. The fourth row shows zoom-in
705 images boxed in the third row. Scale bar: 5 mm. **(d)** The top row shows images of the thermosensitive
706 color-changing sticker attached to the ECCD bottom changing color at the focal point under indicated
707 duration of FUS treatment. The FUS transducer emits continuous waves at a voltage of 40 V. The
708 second row shows zoom-in images of the focal region. The third row shows FITC fluorescence images
709 at the focal point after the termination of FUS treatment. Live dye is used on cells, and non-fluorescent
710 regions reflect cell ablation areas. The fourth row shows zoom-in images boxed in the third row. Scale
711 bar: 5 mm. **(e)** The second image from the left shows the temperature field and cell field at the focal
712 point under FUS exposure with a transducer voltage of 30 V and an exposure time of 3 min. The arrows
713 indicate the size of the focal region along the major and minor axis. The third image is an ellipse fitted
714 to the focal region. **(f)** Line charts showing the lengths of the major and minor axis of the focal region in
715 the temperature field and cell field under different ultrasound intensities (representing different
716 excitation voltages) and different exposure times. **(g)** Scatter plots of the aspect ratio of the focal region
717 in the temperature field and cell field under different ultrasound intensities (*left*), with a line fitted
718 through the least squares method (R^2=0.1753), and scatter plots of the aspect ratio of the focal region in

719 the temperature field and cell field under different FUS treatment duration (*right*), with a line fitted

720 through the least squares method (R^2=0.1322).

721

722

723 **Figure 4**

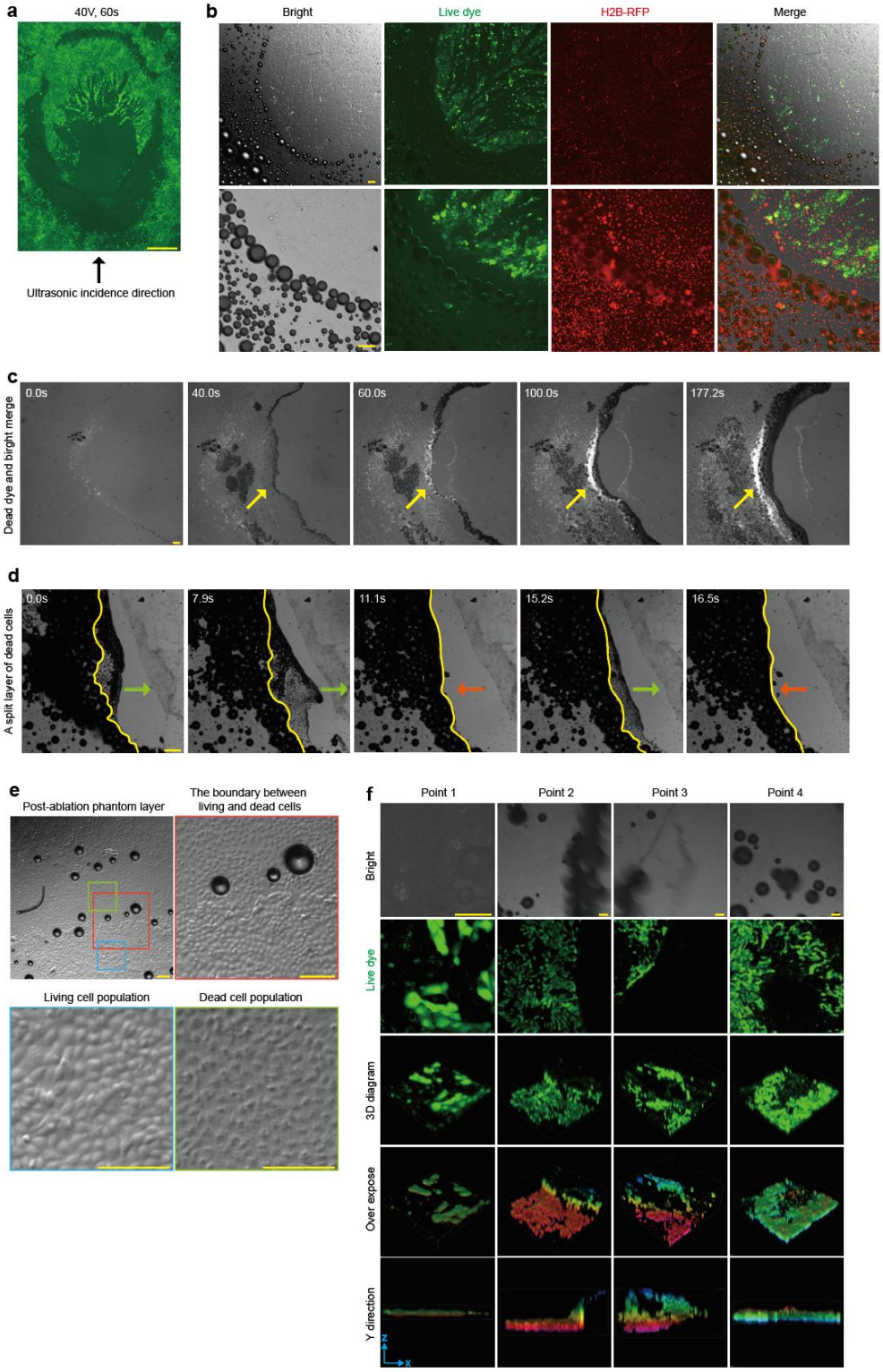

724

725 **Figure 4. Significant association between cell ablation zone and bubble generation zone under**
726 **FUS. (a)** FITC fluorescence images of cells taken after FUS treatment. The FUS transducer is powered
727 at 40 V, emits continuous waves at a frequency of 1 MHz, and has an exposure time of 3 min. The
728 direction of ultrasound incidence is indicated by black arrows. Live dye is used on cells, and non-
729 fluorescent regions reflect the cell ablation zone. Scale bar: 1 mm. **(b)** Bright field, FITC and RFP
730 fluorescence images captured near the focal region after FUS treatment. The FUS transducer is powered
731 at 40 V, emits continuous waves at a frequency of 1 MHz, and has an exposure time of 3 min. Bubbles
732 are opaque and spherical under bright field. H2B-RFP MDCK cells are used. Live dye is used on cells,
733 and non-fluorescent regions reflect the cell ablation zone. Scale bar: 100 μm. **(c)** Time-lapse
734 micrographs captured under bright field and RFP fluorescence during FUS treatment. Yellow arrows
735 indicate bands of bubbles. The FUS transducer is powered at 40 V, emits continuous waves at a
736 frequency of 1 MHz. Cells are stained with red fluorescent dead cell dye, and fluorescent regions reflect
737 the cell ablation zone. Scale bar: 100 μm. (The time-stamp starts from the first image shown here) **(d)**
738 Images captured at the edge of the focal region under bright field during FUS exposure. Yellow lines
739 represent the edges of stable bubble bands. Red and green arrows indicate the expansion and retreat
740 directions of the movement of bubble clusters. The FUS transducer is powered at 40 V, emits continuous
741 waves at a frequency of 1 MHz. Scale bar: 100 μm. (The time-stamp starts from the first image shown
742 here) **(e)** The top-left image shows the bright field microscopic image after ultrasound exposure. The
743 FUS transducer is powered at 40 V, emits continuous waves at a frequency of 1 MHz, and has an
744 exposure time of 3 min. The other three images are zoom-in views of the areas boxed in by different
745 color squares in the top-left image. The bubble zone is spatially correlated with the cell ablation zone,
746 and the morphology of the post-ablation phantom layer (PAPL) after cell ablation is significantly
747 different from the live cell monolayer. Scale bar: 100 μm. **(f)** The top two rows show bright field and
748 FITC fluorescence images after FUS exposure. The FUS transducer is powered at 40 V, emits

749 continuous waves at a frequency of 1 MHz, and has an exposure time of 3 min. Live dye is used on cells,
750 and non-fluorescent regions reflect the cell ablation zone. The bottom three rows show 3D reconstructed
751 microscopic images of the PAPL and its adjacent live cell monolayer. Point 1 shows the PAPL that
752 remained in its original place; Points 2-3 show PAPL rupture and peeled off the substrate by bubbles,
753 along with some live cell monolayer connected to it; Point 4 shows the PAPL forming a "dome" shape,
754 with its central part detached but peripheral part connect to the live cell monolayer on the substrate.
755 Scale bar: 100 μm.
756

757 **Figure 5**

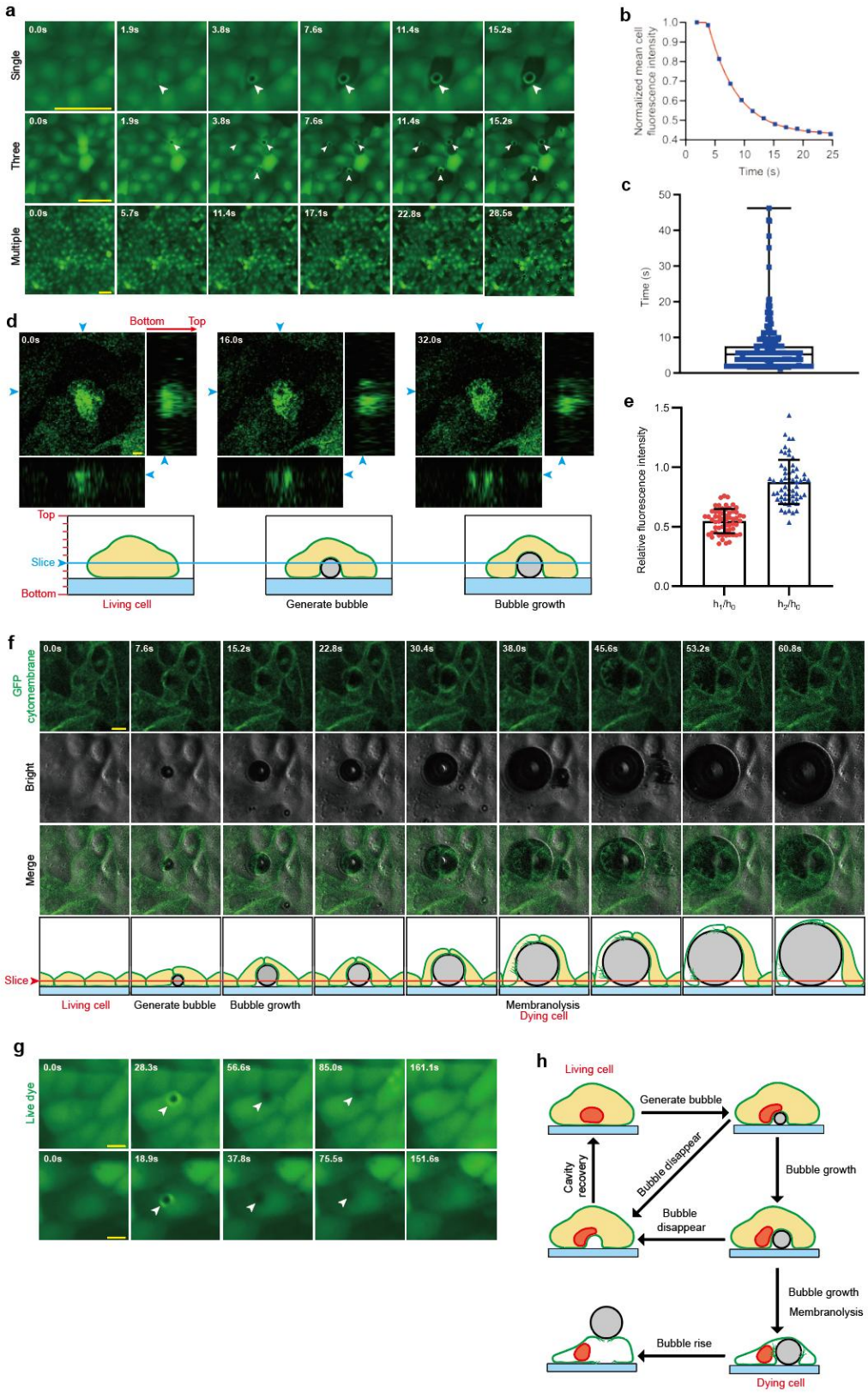

758

759 **Figure 5. Subcellular bubble formation and FUS-induced mechanolysis of the cell. (a)** Time-
760 lapse FITC fluorescence micrographs of MDCK cells under FUS treatment. The three rows represent
761 images where bubbles appear in a single cell, three different cells, and multiple cells, respectively. Live
762 dye is used on cells, and the disappearance of the fluorescent signal reflects cell ablation. The FUS
763 transducer is powered at 40 V, emits continuous waves at a frequency of 1 MHz. Scale bar: 50 μm. **(b)**
764 Scatter plot and interpolated curve showing the average fluorescence intensity of the cell cytoplasm
765 (excluding bubble area) over time for the cells shown in the first row of images in **(a)**. **(c)** Scatter plot of
766 the time taken from bubble appearance to the average fluorescence intensity of the cell dropping to the
767 background fluorescence intensity. (box: 25% - 75%, bar-in-box: median, and whiskers: min and max).
768 n = 3 independent experiments; n_{cell} = 350. The FUS transducer is powered at 40 V, emits continuous
769 waves at a frequency of 1 MHz. **(d)** FITC fluorescence images showing bubbles generated at cells
770 during FUS exposure. The X-Y, X-Z, and Y-Z images were shown for the cell. The green area on the
771 image represents the cell region, and the black area appearing in the cell region represents the bubble
772 region. The intersection points correspond to the center points of the bubbles. Cells are MDCK cells
773 expressing GFP on the cell membrane. The FUS transducer is powered at 40 V, emits continuous waves
774 at a frequency of 1 MHz. Scale bar: 10 μm. **(e)** Analysis of fluorescence intensity at the location of the
775 bubble. The fluorescence intensity at the center of the bubble causing cell ablation is denoted as h_1 when
776 it first appears and h_2 after it caused cell ablation, and the fluorescence intensity at that position before
777 bubble generation is denoted as h_0. The scatter plot shows h_1/h_0 and h_2/h_0. Data were plotted as mean ±
778 s.d. n = 3 independent experiments; $n_{samples}$ = 59. **(f)** Bright field and FITC fluorescence micrographs
779 showing bubbles generated underneath the cell and eventually causing cell membrane rupture during
780 FUS exposure. GFP-cytomembrane MDCK cells were used. Scale bar: 10 μm. **(g)** Time-lapse FITC
781 fluorescence micrographs showing bubbles appearing and disappearing underneath the cell during FUS

treatment. Live dye is added to the cells. The FUS transducer is powered at 40 V, emits continuous waves at a frequency of 1 MHz. Scale bar: 10 μm. **(h)** Schematic of different types of interactions between HIFU-induced bubbles and cells observed in this study.

786 **Figure 6**

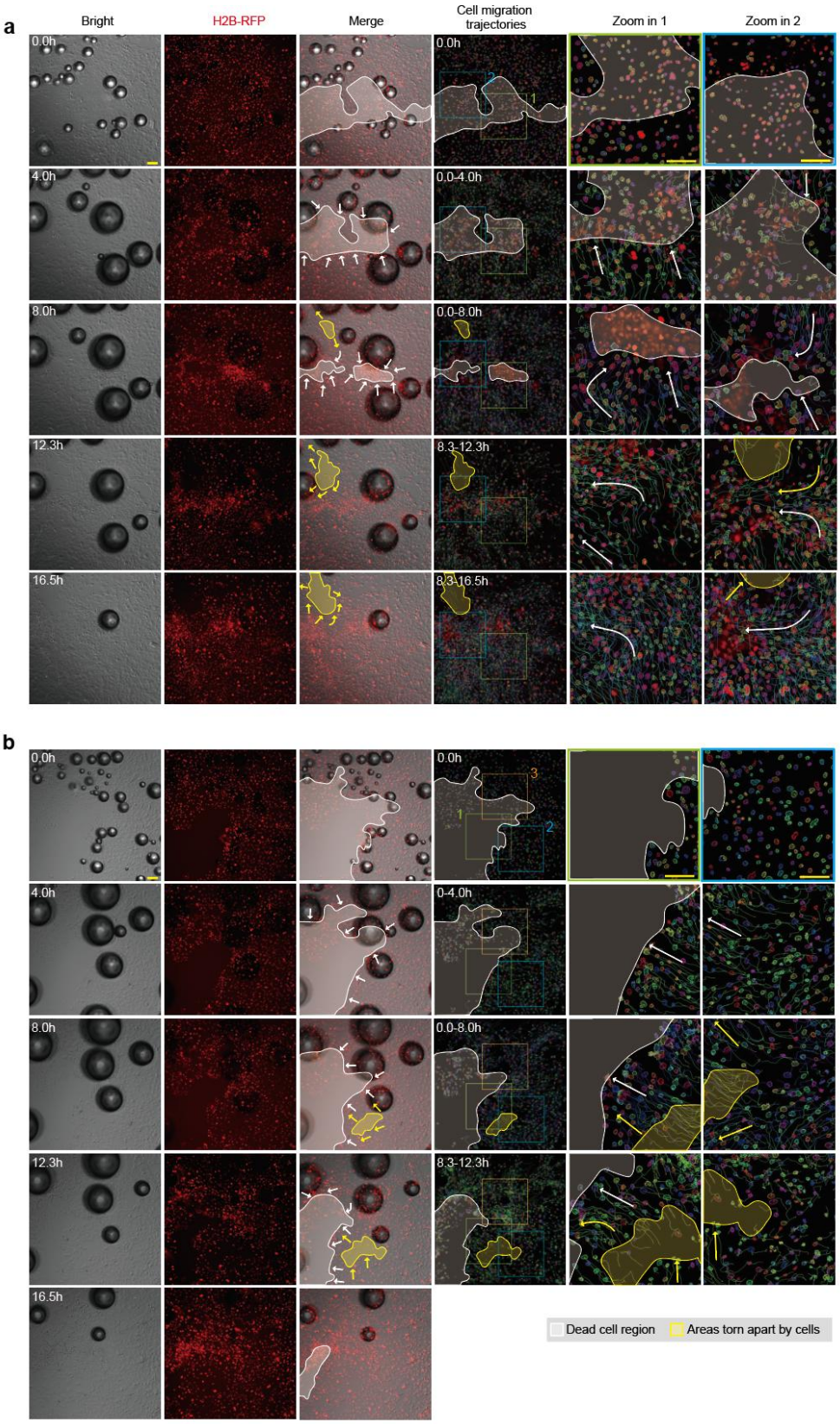

787

788 **Figure 6. Observation of collective cell migration and wound healing after FUS ablation. (a, b)**
789 The first three columns depict time-lapse bright-field and RFP fluorescence micrographs showing the
790 collective migration of live cells towards the PAPL or clear area after HIFU-induced ablation. In the
791 third column, the white area represents the PAPL (with remaining RFP-labeled cell nuclei but no
792 movement) or the clear area (where PAPL detached), with white arrows indicating the direction of
793 collective cell migration. The yellow area represents secondary tissue gaps that appear during the
794 primary wound healing process, largely due to the different directions and speeds of cell migration
795 within the live cell monolayer, with yellow arrows indicating the cell migration direction. The fourth
796 column shows the trajectories of individual cell nuclei during the collective migration (Colored line).
797 The fifth to sixth columns in **(a)** and the fifth to seventh columns in **(b)** provide zoom-in views of the
798 boxed regions in the fourth column. Scale bar: 100 μm. White arrows indicate the location of bubbles.
799

800 **Figure 7**

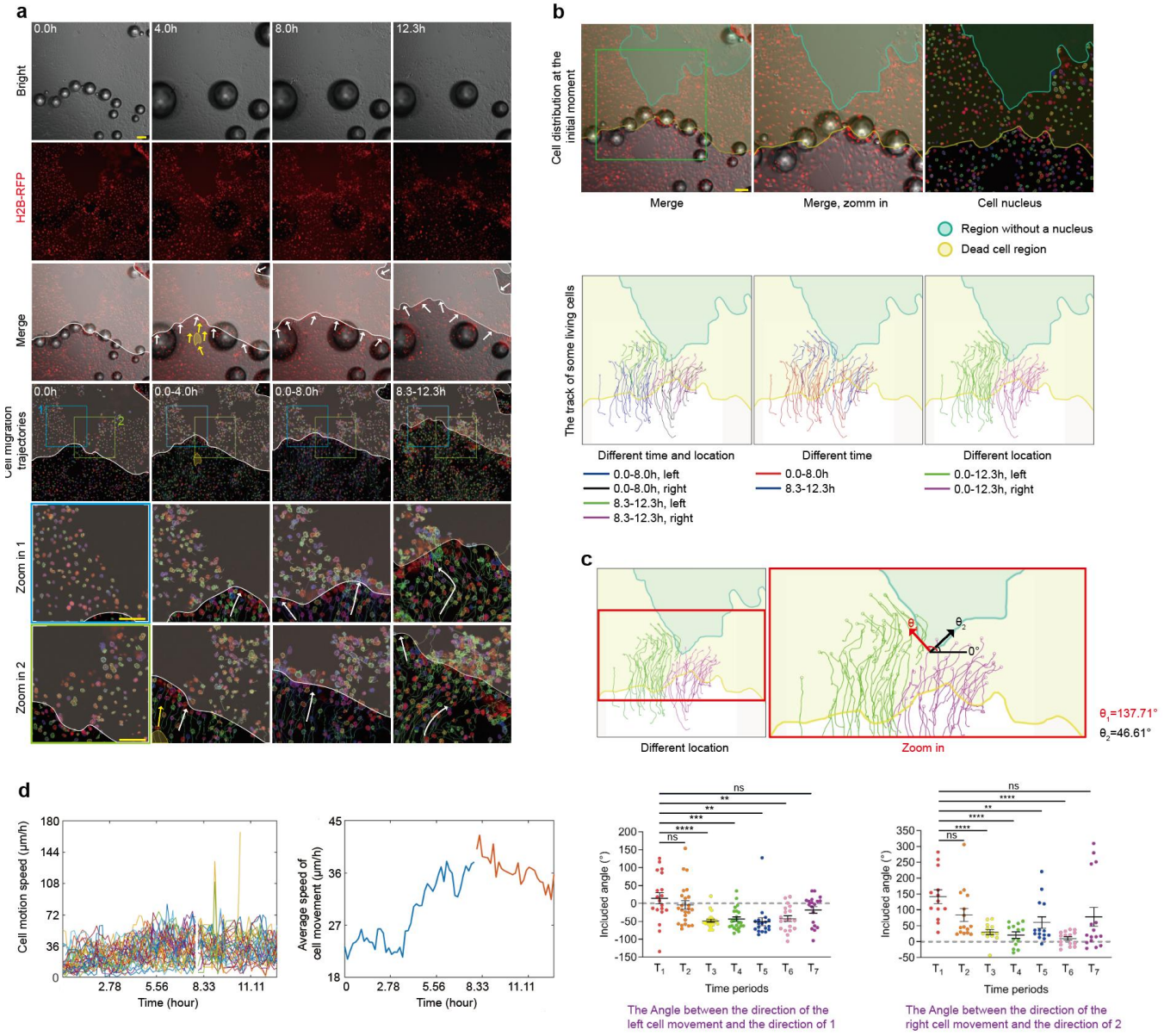

801
802
803 **Figure 6. Effect of the PAPL on the collective migration and wound healing after HIFU-induced**

804 **ablation. (a)** The first three rows show time-lapse bright-field and RFP fluorescence micrographs after

805 focused exposure, illustrating the collective migration of live cells toward the PAPL or the free area

806 (where the PAPL has detached). In the third row, the white area represents the PAPL or the free area,

807 with white arrows indicating cell migration direction. The yellow area represents secondary gaps formed

808 in the collectively migration cell sheet nearby the wound, largely due to different directions and speeds

809 of cells within the monolayer. Yellow arrows indicate the cell migration direction at the edge of the free
810 area. The fourth row displays the trajectories of individual cell nuclei during the wound healing process.
811 The fifth to sixth rows provide zoom-in views of the boxed regions in the fourth row. Scale bar: 100 μm.
812 **(b)** Trajectories of individual cells during collective cell migration. Scale bar: 100 μm. **(c)** Angles
813 between the migration direction of individual cells and the orientation of the interface between the
814 PAPL and the free area at different time points as indicated. (T_1: 0.00-0.67 h; T_2: 2.33-3.00 h; T_3: 4.67-
815 5.33 h; T_4: 7.00-7.67 h; T_5: 8.50-9.17; T_6: 10.17-10.83h; T_7: 11.83-12.50 h). Data were plotted as mean
816 ± s.e.m. * $P < 0.05$, ** $P < 0.01$, *** $P < 0.001$, **** $P < 0.0001$. **(d)** Line graphs depicting the
817 migration speed of individual cells (left) and the average speed of the cell population (right) during
818 collective migration.
819